

Ideal Quantum Geometry for Fractional Chern Insulators

Jennifer Cano^{1,2} and Jie Wang^{3,4}

¹Department of Physics and Astronomy, Stony Brook University, Stony Brook, USA, 11794; email: jennifer.cano@stonybrook.edu

²Center for Computational Quantum Physics, Flatiron Institute, New York, USA, 10010

³International Center for Quantum Materials, Peking University, Beijing, China, 19122; email: jiewang.phy@pku.edu.cn

⁴Beijing Key Laboratory of Quantum Devices, Peking University, Beijing, China, 100871

Xxxx. Xxx. Xxx. Xxx. YYYY. AA:1–27

[https://doi.org/10.1146/\(\(please add article doi\)\)](https://doi.org/10.1146/((please add article doi)))

Copyright © YYYY by the author(s).
All rights reserved

Keywords

Berry curvature, fractional Chern insulator, holomorphic, moiré, quantum geometry, quantum Hall, quantum metric, trace condition.

Abstract

Quantum geometry plays a fundamental role in many aspects of condensed matter physics. Among its central objects are the Berry curvature and the quantum metric – quantities that, while distinct, are intertwined through geometric constraints. In this article, we survey recent progress in understanding when and how this bound is saturated, with particular emphasis on the emergence of momentum-space holomorphicity of Bloch states. These developments highlight a profound connection between certain ideal Bloch bands and the Hilbert space structure of the lowest Landau level. We elucidate this relationship through a review of quantum Hall physics in both homogeneous and spatially varying magnetic fields, and conclude by exploring its implications for the search for fractionalized phases in emerging platforms, including moiré materials.

Contents

1. INTRODUCTION	2
2. QUANTUM GEOMETRY OF BLOCH WAVE FUNCTIONS	3
2.1. Geometric properties of Bloch states	3
2.2. Quantum geometric tensor	4
3. QUANTUM HALL PHYSICS	6
3.1. Landau levels in a uniform magnetic field	6
3.2. Lowest Landau level in an inhomogeneous magnetic field	8
3.3. Landau level wave functions on the torus	10
3.4. Many-body wavefunctions	13
4. IDEAL BANDS	15
4.1. Trace condition and holomorphicity	15
4.2. From holomorphicity to ideal band wavefunctions	16
4.3. Implication of ideal bands for fractional Chern insulators	18
4.4. Examples of ideal bands and experimental relevance	19
5. BEYOND IDEAL BANDS	19
5.1. Deviations from ideality	19
5.2. Orbital embedding	20
5.3. Fractional Chern insulators far from the lowest Landau level	20
6. OUTLOOK	21
7. SUPPLEMENTAL MATERIAL	25
7.1. Geometric bound and null vectors	25
7.2. Translation operator in the lowest Landau level	25
7.3. Kapit-Mueller model	26

1. INTRODUCTION

Quantum geometry provides a fundamental characterization of the local properties of states in parameter space (1, 2, 3, 4, 5). In condensed matter physics, the quantum geometry of single-particle Bloch wave functions parameterized by crystal momentum captures the fundamental mathematical features governing how Bloch wavefunctions are organized and vary across momentum space. Important implications of quantum geometry in condensed matter physics include the modern theory of electric polarization (Berry connection) (6, 7), the anomalous velocity (Berry curvature) (8, 9), and the localization and spread of Wannier functions (quantum metric) (10), among other wide-ranging phenomena. The quantum geometry of many-body states also plays an important role, for instance in explaining the quantization of Hall conductivity (many-body Berry curvature) (11), the optical conductivity sum rules (many-body quantum geometric tensor) (12), and intrinsic and extrinsic dynamics of the fractional quantum Hall effect (13, 14, 15).

Quantum geometry of Bloch states introduces a characteristic length or energy scale, becoming especially significant in narrow-band systems where electron kinetic energy is quenched. Recently, moiré materials have emerged as a class of narrow-band systems in which band dispersion, geometry, and interactions are tunable in situ. In many cases, tuning the material platform, twist angle, and vertical displacement field drives the system into a strongly correlated regime. Various strongly correlated phases of matter have been observed, including superconductivity, correlated insulators, orbital magnetism, and the

first observation of the fractional Chern insulator (FCI) (16, 17, 18).

The FCI is the lattice analog of the fractional quantum Hall (FQH) effect (19, 20, 21, 22, 23). When it exists in zero magnetic field, it is also referred to as the fractional quantum anomalous Hall effect. Although the zero-field FCI was theoretically predicted in 2011, it was not observed until 2023 (24, 25, 26, 27, 28, 29).

In the search for FCIs in band systems, a variety of factors govern their competition with rival phases such as Fermi liquids and charge-ordered states. These include remote-band effects, band dispersion (electron kinetic energy), and electron–electron interactions. Even in the narrow-band limit, the stability of FCIs remains intricately tied to the interplay between band geometry and interactions. Further, the notion of “stability” itself is multifaceted. It first concerns whether the ground state realizes an FCI or a competing phase. If an FCI is the ground state, one may then ask how robust it is, e.g., how large is its energy gap and how robust is it against thermal fluctuations (30, 31). As with other strongly correlated phases, FCI stability is inherently a many-body problem, for which exact criteria are generally elusive except in special solvable limits. Consequently, its study typically relies on a combination of analytical insight and numerical approaches, including exact diagonalization, density matrix renormalization group methods, and diagnostics based on gauge principles and entanglement measures.

From a practical standpoint, a useful – though not essential – strategy for realizing fractionalized phases in 2D systems such as moiré materials is to engineer bands that mimic Landau levels, thereby creating favorable conditions to realize FQH-like physics (32, 22, 30, 33, 34, 35, 36, 37, 38).

In this context, a key question is how to quantify the resemblance of a given narrow band to a Landau level. The emerging consensus is that band geometry – particularly the Berry curvature and quantum metric – play an important role in answering this question. In particular, the so-called trace condition has emerged as a geometric criterion for identifying when a topological band is lowest-Landau-level-like, both in terms of wavefunction structure and the potential to host FCIs as exact ground states. This perspective has proven practically valuable in guiding the search for FCIs in twisted materials. This article reviews recent development in this direction.

2. QUANTUM GEOMETRY OF BLOCH WAVE FUNCTIONS

2.1. Geometric properties of Bloch states

This review focuses on an isolated single band in two dimensions. Denoting the Bloch wavefunction as $\psi_{\mathbf{k}}(\mathbf{r}) = \langle \mathbf{r} | \psi_{\mathbf{k}} \rangle$, Bloch’s theorem prescribes how the wavefunction transforms under lattice translations: $\psi_{\mathbf{k}}(\mathbf{r} + \mathbf{a}) = e^{i\mathbf{k} \cdot \mathbf{a}} \psi_{\mathbf{k}}(\mathbf{r})$. Since Bloch wave functions at different momenta have different translation eigenvalues, they are orthogonal; thus, inner products between Bloch wave functions at different momenta vanish. This is not the case for their cell-periodic parts, $u_{\mathbf{k}}(\mathbf{r}) = \langle \mathbf{r} | u_{\mathbf{k}} \rangle = e^{-i\mathbf{k} \cdot \mathbf{r}} \psi_{\mathbf{k}}(\mathbf{r})$. Thus, the cell-periodic parts of the Bloch wave functions at different momenta can be compared, and this comparison captures the geometric properties of the Bloch band. However, the intrinsic gauge freedom of quantum mechanics, where wavefunctions are defined only up to a phase, renders comparisons subtle.

The Berry connection $\mathbf{A}_{\mathbf{k}} \equiv -i \langle u_{\mathbf{k}} | \nabla_{\mathbf{k}} u_{\mathbf{k}} \rangle$ compares Bloch states by defining parallel transport: given a curve γ in the Brillouin zone (BZ), states $|u_{\mathbf{k}}\rangle$ with $\mathbf{k} \in \gamma$ are said to be parallel if $\mathbf{A}_{\mathbf{k}} = 0$ at all points along this curve. It is always possible to choose a gauge satisfying this condition: breaking the curve into discrete pieces, parallel transport amounts

to choosing the phase of $u_{\mathbf{k}_{n+1}}$ such that $\langle u_{\mathbf{k}_{n+1}} | u_{\mathbf{k}_n} \rangle > 0$ is real and positive.

Parallel transport also defines the derivative operator. Since the phase at different momenta is not uniquely defined, only comparisons between parallel states are meaningful. This is accomplished by the covariant derivative operator $D^a = \partial_{k_a} - iA_{\mathbf{k}}^a$, which satisfies $\langle u_{\mathbf{k}} | D^a u_{\mathbf{k}} \rangle = 0$. In the single-band case we consider here, under the gauge transformation $|u_{\mathbf{k}}\rangle \rightarrow e^{i\theta_{\mathbf{k}}} |u_{\mathbf{k}}\rangle$, the derivative operator also transforms as $|D^a u_{\mathbf{k}}\rangle \rightarrow e^{i\theta_{\mathbf{k}}} |D^a u_{\mathbf{k}}\rangle$.

The crucial subtlety is that along a closed loop γ , the parallel-transported state need not return with the same phase as the initial state. Such a phase difference between the initial state and the final state after parallel transport along a closed loop is called the Berry phase. The Berry phase is gauge independent, and, by Stokes' theorem, is determined by the integration of Berry curvature density inside the loop. Specifically, if $|u_{\mathbf{k}_f}\rangle$ and $|u_{\mathbf{k}_i}\rangle$ denote the final and initial states parallel-transported around γ ,

$$|u_{\mathbf{k}_f}\rangle = e^{i \oint_{\gamma} \mathbf{A}_{\mathbf{k}} \cdot d\mathbf{k}} |u_{\mathbf{k}_i}\rangle = e^{i \iint_{M_+} d^2\mathbf{k} \Omega_{\mathbf{k}}} |u_{\mathbf{k}_i}\rangle = e^{-i \iint_{M_-} d^2\mathbf{k} \Omega_{\mathbf{k}}} |u_{\mathbf{k}_i}\rangle, \quad 1.$$

where M_{\pm} are, respectively, the inner and outer surfaces bounded by the loop γ and $\Omega_{\mathbf{k}} = \nabla \times \mathbf{A}_{\mathbf{k}}$ is the Berry curvature. The choice of M_+ or M_- should not matter, which immediately implies the quantization of the Chern number,

$$C = \frac{1}{2\pi} \int d^2\mathbf{k} \Omega_{\mathbf{k}} \in \mathbb{Z}, \quad 2.$$

which measures the total Berry curvature integrated over the BZ torus.

To summarize: geometrically, the Berry phase characterizes the difference between a state and its parallel-transported counterpart after traversing a closed loop, Berry curvature measures the density of Berry phase, and a non-vanishing Chern number implies the absence of a globally defined smooth gauge choice for the Bloch states.

Having discussed phase, we now turn to the ‘‘distance’’ between quantum states. A measure of distance $d(\mathbf{k}, \mathbf{k}')$ must satisfy three conditions: symmetry $d(\mathbf{k}, \mathbf{k}') = d(\mathbf{k}', \mathbf{k})$; non-negativity $d(\mathbf{k}, \mathbf{k}') \geq 0$; and the triangle inequality $d(\mathbf{k}, \mathbf{k}') + d(\mathbf{k}', \mathbf{k}'') \geq d(\mathbf{k}, \mathbf{k}'')$. The *quantum distance* between Bloch states is defined by $d(\mathbf{k}, \mathbf{k}') \equiv 1 - |\langle u_{\mathbf{k}} | u_{\mathbf{k}'} \rangle|^2$, which takes values in $[0, 1]$ (assuming the Bloch state is normalized). Expanding the distance for nearby points gives the *quantum metric*,

$$d(\mathbf{k}, \mathbf{k} + \delta\mathbf{k}) = \sum_{ab} g_{\mathbf{k}}^{ab} \delta k_a \delta k_b + \dots, \quad 3.$$

where $a, b = x, y$ denotes the spatial directions.

2.2. Quantum geometric tensor

The quantum metric, Berry curvature and covariant derivative are nicely organized together in the so-called *quantum geometric tensor* (QGT). In the single band case, the QGT is defined as the inner product of covariant derivative of Bloch states,

$$Q_{\mathbf{k}}^{ab} = \langle D_{\mathbf{k}}^a u_{\mathbf{k}} | D_{\mathbf{k}}^b u_{\mathbf{k}} \rangle = g_{\mathbf{k}}^{ab} + \frac{i}{2} \epsilon^{ab} \Omega_{\mathbf{k}}, \quad 4.$$

where ϵ^{ab} is the anti-symmetric tensor. The QGT is gauge invariant and Hermitian, so that it has a real symmetric part and imaginary anti-symmetric part, which are, respectively, the quantum metric and the Berry curvature. The QGT is also positive semi-definite, i.e., for any vector (c_1, c_2) , $c_a^* Q_{\mathbf{k}}^{ab} c_b = \langle \chi | \chi \rangle \geq 0$, where $|\chi\rangle = c_a |D^a u_{\mathbf{k}}\rangle$.

2.2.1. Coordinate dependence and complex structure. The QGT transforms covariantly under coordinate transformations. Specifically, under a coordinate transformation $x_a \rightarrow x'_a = \Lambda_{ab}x_b$, with $\det \Lambda = 1$, $(Q^{ab})' = \Lambda^{ac}\Lambda^{bd}Q^{cd}$. From Eq. 4., g transforms the same way as Q , while Ω is unchanged (22, 30).

Given a metric h_{ab} , with $\det h = 1$, a natural coordinate transformation is given by factorizing it into vectors $e^{1,2}$ (the vielbeins) satisfying

$$h_{ab} = \delta_{ij}e_a^i e_b^j, \quad \epsilon_{ab} = \epsilon_{ij}e_a^i e_b^j, \quad 5.$$

which fixes the vectors' length and orientation. In the transformed coordinates $\tilde{x}^i = e_a^i x^a$, the ellipse defined by $h_{ab}r^a r^b = R^2$ becomes a circle $\delta_{ij}\tilde{x}^i \tilde{x}^j = R^2$.

Such a coordinate transformation also introduces a *complex structure* that will be employed frequently in the subsequent discussion of quantum Hall physics. A complex structure is a bijective map from the two-dimensional plane \mathbb{R}^2 to the complex plane \mathbb{C}^1 ; a natural choice is $z = (\tilde{x}^1 + i\tilde{x}^2)/\sqrt{2}$. In the original coordinates, the complex structure is defined concisely by $x \mapsto z = w_a x^a$ (13), where $w_a = (e_a^1 + ie_a^2)/\sqrt{2}$. Eq. 5. then yields:

$$h_{ab} = w_a^* w_b + w_a w_b^*, \quad i\epsilon_{ab} = w_a^* w_b - w_a w_b^*. \quad 6.$$

Eq. 6. uniquely fixes the complex structure defined by h up to a global $U(1)$ phase transformation $w_a \rightarrow e^{i\phi} w_a$. For later use, we introduce the identities

$$w^a w_a^* = 1, \quad w^a w_a = 0, \quad 7.$$

where the indices are raised/lowered by the metric, with $h^{ab}h_{bc} = \delta_c^a$.

2.2.2. Embedding dependence. In tight-binding models with multiple orbitals per unit cell, we refer to changes in the relative positions of orbitals within the unit cell as modifications of the orbital embedding. The QGT is *not* invariant under a change in the orbital embedding (39, 31, 40). Generically, a change in embedding adds an extra term to the Berry connection, $\delta\mathbf{A}_{\mathbf{k}}$, which leads to a non-vanishing change to both the metric and the Berry curvature. (The latter is given by $\nabla \times \delta\mathbf{A}_{\mathbf{k}}$; Stokes' theorem ensures that the Chern number in Eq. 2. is unchanged.) We return to the importance of the embedding dependence in Sec. 5.2.

2.2.3. Geometrical bounds. The real and imaginary parts of the QGT are not independent. Specifically, the Berry curvature lower-bounds the metric as follows:

$$\text{Tr}_h g_{\mathbf{k}} \geq 2\sqrt{\det g_{\mathbf{k}}} \geq |\Omega_{\mathbf{k}}|, \quad 8.$$

for any positive-definite determinant-one symmetric matrix h . In Eq. 8., we have defined a generalized trace, $\text{Tr}_h g = \sum_{ab} h_{ab} g^{ab}$, which is connected to the basis transformation described in Sec. 2.2.1: specifically, defining $Q' = \Lambda Q \Lambda^T$, $\text{Tr} Q' = \text{Tr}_h Q$ with $h = \Lambda^T \Lambda$. The proof of the geometric bound in Eq. 8. is reviewed in the Supplemental Material (SM) Sec. 7.1. It is equivalent to the integrated version,

$$\frac{1}{2\pi} \int d^2 \mathbf{k} \text{Tr}_h g_{\mathbf{k}} \geq \frac{1}{2\pi} \int d^2 \mathbf{k} 2\sqrt{\det g_{\mathbf{k}}} \geq C. \quad 9.$$

3. QUANTUM HALL PHYSICS

3.1. Landau levels in a uniform magnetic field

In this section, we derive the Landau level wave functions on the plane in a spatially uniform magnetic field, which establishes the notation for our subsequent derivations of the wave functions in a spatially varying field (Sec. 3.2) and on the torus (Sec. 3.3), as well as of the many-body wave functions (Sec. 3.4). Much of the material in this section can also be found in several excellent reviews of quantum Hall physics (41, 42, 15, 43, 44).

The conventional model for quantum Hall physics starts with the effective theory describing the low energy dispersion of a quadratic band,

$$H_{\text{band}} = \frac{1}{2} (m^{-1})^{ab} p_a p_b, \quad 10.$$

where $p_a = -i\hbar\partial_a$ is the canonical momentum operator and m_{ab} is the mass tensor. Factoring out its determinant, $|m| = \sqrt{\det m}$, yields a unimodular metric describing its shape,

$$(m^{-1})^{ab} = \frac{1}{|m|} g^{ab}, \quad 11.$$

where $\det g = 1$.

Upon applying an external magnetic field, the canonical momentum operator is replaced by the dynamical momentum operator π_a through minimal coupling,

$$p_a \rightarrow \pi_a(\mathbf{r}) = p_a - eA_a(\mathbf{r}), \quad 12.$$

where $A_a(\mathbf{r})$ is the vector gauge potential whose curl is the magnetic field. Throughout this work, we specialize to two dimensions (2D) and consider a magnetic field normal to the 2D plane so that $\mathbf{B}(\mathbf{r}) = B(\mathbf{r})\hat{z}$ and $\hat{z} \cdot [\nabla \times \mathbf{A}(\mathbf{r})] = B(\mathbf{r})$.

In this section, we consider a uniform magnetic field, so that $B(\mathbf{r}) = B$. We choose a convention where $B < 0$ and electric charge $e < 0$, so that the combination $eB > 0$. The magnetic length is defined by $\ell_B = \sqrt{\hbar/(eB)}$. The momentum operators have a nontrivial but simple commutator,

$$[\pi_a, \pi_b] = i\hbar^2 \epsilon_{ab} / \ell_B^2. \quad 13.$$

The uniform field model can be solved exactly by transforming the dynamical momentum operators (π_x, π_y) into a set of canonical ladder operators $(\hat{a}_h, \hat{a}_h^\dagger)$. Since the ladder operators will be determined by a metric, we add the subscript h . Following the notation of the complex structure in Eq. 6., we define,

$$\hat{a}_h = \frac{\ell_B}{\hbar} w^a(h) \pi_a, \quad \hat{a}_h^\dagger = \frac{\ell_B}{\hbar} [w^a(h)]^* \pi_a, \quad 14.$$

which satisfy $[\hat{a}_h, \hat{a}_h^\dagger] = 1$. Different choices of h amount to performing a Bogoliubov transformation on the ladder operators (13).

Rewriting the Hamiltonian in Eq. 10. in terms of \hat{a}_h and \hat{a}_h^\dagger generically contains linear combinations of \hat{a}_h^2 , $\hat{a}_h^{\dagger 2}$, $\hat{a}_h^\dagger \hat{a}_h$ and $\hat{a}_h \hat{a}_h^\dagger$. The model is brought into diagonal form (i.e., without \hat{a}_h^2 and $\hat{a}_h^{\dagger 2}$ terms) only for the specific choice $h^{ab} = g^{ab}$. In that case, the Hamiltonian reads,

$$H = \hbar\omega_c \left(\hat{a}_g^\dagger \hat{a}_g + \frac{1}{2} \right) + \frac{1}{2} g\mu_B B, \quad 15.$$

where $\omega_c = eB/|m|$ is the cyclotron frequency and we have added the second term to incorporate the Zeeman splitting, with g indicating the g -factor (the distinction with the metric g should be clear from context). For notational simplicity, we now drop the subscript g on the ladder operators.

Eq. 15. immediately yields the Landau level energies and eigenvectors. We now focus on the “ $g = 2$ ” case, defined by $g = 2m_e/|m|$, with m_e the electron mass. In this case, the last two terms cancel (recall our convention is $e, B < 0$, and, as always, $\mu_B = |e|\hbar/2m_e$); thus the energy of the n^{th} Landau level is $E_n = n\hbar\omega_c$. The eigenvectors are constructed in the usual way: the $n = 0$ states are called the lowest Landau level (LLL), denoted by $|0\rangle$, and are annihilated by \hat{a} . The n^{th} Landau level state is constructed from the lowest one by

$$|n\rangle = \frac{(\hat{a}^\dagger)^n}{\sqrt{n!}}|0\rangle. \quad 16.$$

The LLL wave functions can be found explicitly by working in the symmetric gauge where $A_a(\mathbf{r}) = -B\epsilon_{ab}r^b/2$, and using the identities in Eq. 7. to write Eq. 14. as

$$\hat{a} = -i\left(\ell_B\partial_{\bar{z}} + \frac{z}{2\ell_B}\right), \quad \hat{a}^\dagger = i\left(-\ell_B\partial_z + \frac{\bar{z}}{2\ell_B}\right) \quad 17.$$

where the complex coordinate z is defined by $z = w_a(g)r^a$, $\partial_{\bar{z}} = w^a(g)\partial_a$, and $\bar{z} \equiv z^*$. It follows that the wave functions annihilated by \hat{a} are given by a holomorphic function (i.e., a function only of z , not \bar{z}), multiplied by a Gaussian,

$$\psi_{\text{LLL}}(\mathbf{r}) = f(z) \exp\left(-\frac{1}{2}|z|^2/\ell_B^2\right). \quad 18.$$

Inside each Landau level, the states are highly degenerate. Their degeneracy can be resolved by symmetries, as we now explain. The quantum mechanical analog of the classical cyclotron radius is $\bar{R}^a = -\epsilon^{ab}\pi_b\ell_B^2/\hbar$, which defines a guiding center operator

$$R^a = r^a - \bar{R}^a = r^a + \epsilon^{ab}\pi_b\ell_B^2/\hbar. \quad 19.$$

From the commutator of dynamical momentum in Eq. 13., the guiding centers obey $[R^a, R^b] = -i\ell_B^2\epsilon^{ab}$. Analogous to the Landau orbital ladder operators $\hat{a}_h, \hat{a}_h^\dagger$, the guiding center operators combined with a choice of metric define guiding center ladder operators,

$$\hat{b}_h = [w_a(h)]^* R^a/\ell_B, \quad \hat{b}_h^\dagger = w_a(h)R^a/\ell_B, \quad 20.$$

which satisfy $[\hat{b}_h, \hat{b}_h^\dagger] = 1$. The differential operators are given explicitly by

$$\hat{b} = \ell_B\partial_z + \frac{\bar{z}}{2\ell_B}, \quad \hat{b}^\dagger = -\ell_B\partial_{\bar{z}} + \frac{z}{2\ell_B}, \quad 21.$$

where again the complex coordinate z is defined from the complex structure associated to the unimodular metric h .

Since the guiding center ladder operators commute with the Hamiltonian, they can resolve the degeneracy of each Landau level. The symmetry of the manifold determines how to do so. On the infinite plane or the sphere, which have continuous rotation symmetry, the degeneracy is resolved by rotational angular momentum m , while on the cylinder or torus, which have translation symmetry, the momentum \mathbf{k} resolves the degeneracy.

3.2. Lowest Landau level in an inhomogeneous magnetic field

In a homogeneous magnetic field, the Zeeman term shifts the energy levels uniformly. If the g -factor happens to be $g = 2$, then the LLL sits exactly at zero energy. We now prove a rather surprising fact: even in a spatially varying magnetic field, at $g = 2$, the LLL remains flat and pinned exactly to zero energy (45, 15).

We split the inhomogeneous magnetic field, $\mathbf{B}(\mathbf{r})$, into its uniform part, \mathbf{B} , and its spatially varying part, $\delta\mathbf{B}(\mathbf{r})$, which averages to zero. We use $A_a(\mathbf{r})$ to denote the vector potential associated with the uniform part of the magnetic field, which, without loss of generality, can be written in symmetric gauge as $A_a(\mathbf{r}) = -B\epsilon_{ab}r^b/2$, and use $\delta A_a(\mathbf{r})$ to denote the vector potential associated with the spatially varying part of the magnetic field. Since $\delta\mathbf{B}(\mathbf{r})$ integrates to zero, $\delta\mathbf{B}$ and $\delta\mathbf{A}$ can be written in terms of a scalar field ϕ as

$$\delta A_a(\mathbf{r}) = -\epsilon_{ab}g^{bc}\partial_c\phi(\mathbf{r}), \quad \delta B(\mathbf{r}) = g^{ab}\partial_a\partial_b\phi(\mathbf{r}) \equiv \Delta_{\mathbf{r}}\phi(\mathbf{r}), \quad 22.$$

where $\Delta_{\mathbf{r}} = g^{ab}\partial_a\partial_b$ is the Laplacian operator. When the full magnetic field can be written as the Laplacian of a scalar potential, i.e., $\mathbf{B}(\mathbf{r}) = \frac{\hbar}{e}\Delta_{\mathbf{r}}K(\mathbf{r})$, we refer to $K(\mathbf{r})$ as the Kähler potential. In the present case,

$$K(\mathbf{r}) = \frac{1}{4l_B^2}g_{ab}r^a r^b + \frac{e}{\hbar}\phi(\mathbf{r}) = \frac{1}{2l_B^2}|z|^2 + \frac{e}{\hbar}\phi(\mathbf{r}). \quad 23.$$

Denoting the dynamical momentum of the inhomogeneous field as $\pi_a(\mathbf{r})$ and using π_a to denote the momentum in the uniform magnetic field,

$$\pi_a(\mathbf{r}) = \pi_a - e\delta A_a(\mathbf{r}) = \pi_a + e\epsilon_{ab}g^{bc}\partial_c\phi(\mathbf{r}), \quad 24.$$

whose commutator now depends on the total magnetic field,

$$[\pi_a(\mathbf{r}), \pi_b(\mathbf{r})] = ie\hbar\epsilon_{ab}B(\mathbf{r}). \quad 25.$$

We now consider the $g = 2$ problem in such an inhomogeneous magnetic field, described by the Hamiltonian

$$H = \frac{1}{2m}g^{ab}\pi_a(\mathbf{r})\pi_b(\mathbf{r}) + \frac{1}{2}g\mu_B B(\mathbf{r}). \quad 26.$$

The spatial dependence of the commutator in Eq. (25) makes the model in Eq. (26) impossible to solve analytically. Despite this difficulty, we will show that the zero mode remains, i.e., the LLL remains completely degenerate.

To start, we use the complex structure w_a associated with the mass tensor (i.e., the complex structure defined in Eq. 6. with the metric g_{ab} given in Eq. 11.) to introduce the holomorphic and anti-holomorphic momentum operators,

$$\pi^-(\mathbf{r}) = w^a\pi_a(\mathbf{r}), \quad \pi^+(\mathbf{r}) = (w^a)^*\pi_a(\mathbf{r}), \quad 27.$$

which are analogous to the operators in Eq. 14., but have a spatially varying commutator,

$$[\pi^-(\mathbf{r}), \pi^+(\mathbf{r})] = e\hbar B(\mathbf{r}). \quad 28.$$

Using these operators, the Hamiltonian in Eq. 26. can be rewritten as:

$$H = \frac{1}{m}\pi^+(\mathbf{r})\pi^-(\mathbf{r}). \quad 29.$$

Thus, the kernel of $\pi^-(\mathbf{r})$ is precisely the zero energy eigenspace of H . The dimension of this space is unchanged by the varying magnetic field because the $\pi^-(\mathbf{r})$ operator is related to its counterpart in the uniform field, $\pi^- = \hat{a}\hbar/\ell_B = -i\hbar\bar{\partial} - i\hbar z/(2\ell_B^2)$, by the similarity transform

$$\pi^-(\mathbf{r}) = w^a \pi_a(\mathbf{r}) = \pi^- - ie\bar{\partial}\phi(\mathbf{r}) = e^{-\frac{e}{\hbar}\phi(\mathbf{r})} \pi^- e^{\frac{e}{\hbar}\phi(\mathbf{r})}. \quad 30.$$

Hence, if $|0\rangle$ denotes the state annihilated by π^- in a homogeneous magnetic field, then $e^{-e\phi(\mathbf{r})/\hbar}|0\rangle$ will be annihilated by $\pi^-(\mathbf{r})$ in an inhomogeneous field, and thus is a zero energy eigenstate of the Hamiltonian in Eq. 29.. It follows that the entire LLL remains exactly at zero energy in an inhomogeneous field. In terms of the Kähler potential introduced in Eq. 23., Eq. 30. also implies that the LLL wave function in Eq. 18. can be written as

$$\psi_{\text{LLL}}(\mathbf{r}) = f(z)e^{-K(\mathbf{r})}, \quad 31.$$

which applies to both the homogeneous or inhomogeneous magnetic field cases. We note that the degenerate LLL is a unique feature of the zeroth Landau level: in an inhomogeneous field, the higher Landau levels are not flat in energy.

3.2.1. Dirac Landau levels in magnetic field. We now briefly compare the charged particle in a magnetic field to the 2D Dirac fermion in a magnetic field, which is closely related to the $g = 2$ quantum Hall problem just described. We will show that it also has a flat LLL that survives spatial variation in the magnetic field. Physically, the model can be realized at the interface between a Type II superconductor and a Dirac material such as graphene or a topological insulator surface (46).

A 2D Dirac fermion in a non-uniform magnetic field is described by the Hamiltonian:

$$H_{\text{Dirac}} = v_F \sum_{i=1,2} \sum_{a=x,y} \frac{1}{\sqrt{2}} \sigma^i e_i^a \pi_a(\mathbf{r}) = v_F \begin{pmatrix} & \pi^+(\mathbf{r}) \\ \pi^-(\mathbf{r}) & \end{pmatrix}, \quad 32.$$

where e_i^a is the frame field introduced in Sec. 2.2.1, which accommodates an anisotropic Dirac cone. When the magnetic field is uniform, the above model reduces to the standard problem, which exhibits a zero mode and a particle-hole symmetric energy spectrum, $E_n = \pm\hbar v_F/\ell_B \sqrt{n}$, describing the famous Landau level spectrum of graphene (47, 48, 49, 50). When the magnetic field is spatially modulated, the full spectrum cannot be found analytically. However, the zero mode can be found by squaring the Hamiltonian:

$$H_{\text{Dirac}}^2 = v_F^2 \begin{pmatrix} \pi^+(\mathbf{r})\pi^-(\mathbf{r}) & 0 \\ 0 & \pi^-(\mathbf{r})\pi^+(\mathbf{r}) \end{pmatrix} \quad 33.$$

The upper quadrant is precisely the $g = 2$ quantum Hall problem in Eq. 29. Hence, the zero mode survives the spatially modulated field, and its wave functions are given by

$$\tilde{\Psi}_0 = \begin{pmatrix} f(z) \\ 0 \end{pmatrix} e^{-K(\mathbf{r})}, \quad 34.$$

where $K(\mathbf{r})$ is the Kähler potential in Eq. 23.. Eq. 34. is a spinor-generalization of Eq. 31..

3.3. Landau level wave functions on the torus

The quantum Hall problem on the torus describes electrons on a 2D manifold with periodic boundary conditions in both directions and a uniform perpendicular magnetic field. Since the torus is a special case of the infinite plane with boundaries identified, the LLL states on the torus must also be holomorphic functions, locally identical to Eq. 18.. However, the periodicity strongly constrains the analytical form of the global wave function (51, 52).

3.3.1. Boundary conditions and translation operators. First, the torus geometry requires the magnetic flux quanta be an integer, N_ϕ , due to the Dirac quantization condition. Because each flux corresponds to an area of $2\pi l_B^2$, the torus area must be,

$$\hat{z} \cdot (\mathbf{L}_1 \times \mathbf{L}_2) = 2\pi N_\phi l_B^2, \quad 35.$$

where \mathbf{L}_1 and \mathbf{L}_2 are respectively the two primitive real space vectors spanning the torus and \hat{z} is the unit vector normal to the torus surface. We orient the vectors such that $\mathbf{L}_1 \times \mathbf{L}_2$ is positive. To fully specify the quantum Hall problem on the torus requires, in addition to the primitive vectors, boundary conditions,

$$t(\mathbf{L}_i)|\psi\rangle = e^{i\theta_i}(-1)^{N_\phi}|\psi\rangle, \quad 36.$$

where $t(\mathbf{L}_i)$ is the translation operator that transports an electron around the torus and $0 \leq \theta_{i=1,2} < 2\pi$. The boundary conditions can be interpreted as threading fictitious flux through a hole of the torus, so that θ_i is simply the Berry phase acquired by an electron transported around the torus cycle.

To understand the constraint of the boundary condition in Eq. 36. requires the action of translation operators in the LLL. The magnetic translation operator that transports an electron by a distance \mathbf{d} is given by,

$$t(\mathbf{d}) = \exp(i\mathbf{d} \times \mathbf{R}/\ell_B^2) = \exp\left[(d^* \hat{b}^\dagger - d\hat{b})/\ell_B\right], \quad 37.$$

where $d = w_a d^a$ is the complex coordinate of \mathbf{d} . In the LLL, the translation operator acts by (see SM Sec. 7.2),

$$t(\mathbf{d})\psi_{\text{LLL}}(\mathbf{r}) = e^{\frac{1}{2}(z\bar{d} - \bar{z}d)/\ell_B^2} \psi_{\text{LLL}}(\mathbf{r} - \mathbf{d}), \quad 38.$$

where $\psi_{\text{LLL}}(\mathbf{r}) = f(z) \exp(-|z|^2/2l_B^2)$. Thus, the translation operators do not commute, and their non-commutativity is determined by the Berry phase accumulated by an electron traversing the closed loop spanned by \mathbf{d} and \mathbf{d}' :

$$t(\mathbf{d})t(\mathbf{d}') = e^{i\mathbf{d} \times \mathbf{d}'/l_B^2} t(\mathbf{d}')t(\mathbf{d}). \quad 39.$$

As mentioned below Eq. 36., physically $t(\mathbf{d})$ can be achieved by fictitious flux insertion. Since, by gauge invariance, the Hilbert space is only invariant under insertion of integer flux, the allowed translations must be discrete and commute with $t(\mathbf{L}_i)$. Thus, the elementary magnetic translation group elements are given by $\hat{t}_i = t(\mathbf{L}_i/N_\phi)$; their commutation relation $\hat{t}_1\hat{t}_2 = \exp(2\pi i/N_\phi)\hat{t}_2\hat{t}_1$ implies an N_ϕ degeneracy of each Landau level.

Combining the form of the wave function in Eq. 18. with the boundary condition in Eq. 36., and applying the action of the translation operator in Eq. 38. yields

$$f(z + L_i) = e^{-i\theta_i} e^{\varphi_i(z)} (-1)^{N_\phi} f(z), \quad 40.$$

where L_i is the complex coordinate of the primitive torus vectors and $\varphi_i(z) = L_i^*(z + L_i/2)/\ell_B^2$, which is holomorphic in z , as required.

3.3.2. Lowest Landau level wavefunctions on the torus. The boundary condition in Eq. 40 combined with the expression for the torus area in Eq. 35. can be used to evaluate the following contour integral around the torus (51, 52),

$$\frac{1}{2\pi i} \oint dz \partial_z \ln [f(z)] = \frac{1}{2\pi i} \left[\int_0^{L_1} dz \partial_z \ln \frac{f(z)}{f(L_2+z)} + \int_0^{L_2} dz \partial_z \ln \frac{f(L_1+z)}{f(z)} \right] = N_\phi. \quad 41.$$

This implies that each LLL wavefunction on the torus must have N_ϕ zeros. The periodicity and locations of the zeros uniquely fix the analytical form of the LLL wavefunction on the torus: for zeros at positions $\omega_1, \dots, \omega_{N_\phi}$, the wave function can be written as (53, 54),

$$\Phi_\omega(\mathbf{r}) = \left[\prod_{i=1}^{N_\phi} e^{\omega_i^* z / (N_\phi \ell_B)} \tilde{\sigma}(z - \omega_i) \right] e^{-\frac{1}{2}|z|^2 / \ell_B^2}, \quad 42.$$

where $\tilde{\sigma}(z)$ denotes the modified Weierstrass sigma function (55) (a holomorphic function containing one zero in the fundamental domain) with the following quasi-periodicity

$$\tilde{\sigma}(z + L_i) = -e^{L_i^* (z + \frac{L_i}{2}) / (N_\phi \ell_B^2)} \tilde{\sigma}(z). \quad 43.$$

The Weierstrass sigma function is used instead of the Jacobi theta function because it has more compact translation properties and is modular invariant.

However, the positions of the zeros cannot be chosen arbitrarily: their sum is constrained by the boundary conditions on the torus to satisfy

$$\square \equiv \sum_{n=1}^{N_\phi} \omega_n = \frac{\theta_1}{2\pi} L_2 - \frac{\theta_2}{2\pi} L_1 \pmod{L}, \quad 44.$$

where mod L indicates that the equality should be taken modulo integer multiples of L_1 and L_2 . This constraint is derived by first inserting the boundary condition of the sigma function in Eq. 43. into the wave function in Eq. 42. and then comparing to the boundary condition on $f(z)$ in Eq. 40., which yields $\theta_i = -i (L_i^* \square - L_i \square^*) / N_\phi \pmod{2\pi}$. One then arrives at Eq. 44. by comparison to the equation for the torus area in Eq. 35. written in complex coordinates, i.e., $L_1^* L_2 - L_1 L_2^* = 2\pi i N_\phi \ell_B^2$.

3.3.3. Bloch Landau level states. Our motivation for reviewing the LLL states on the torus is for comparison to Bloch bands and, in particular, ideal bands. Since Bloch's theorem prescribes that eigenstates in a Bloch band are classified by their translation properties, to complete the comparison requires the translation eigenstates in the LLL, which is a subtle question due to the magnetic field.

To apply Bloch's theorem requires a lattice of "magnetic unit cells," each containing integer flux per cell, so that the translation operators commute. While the quantum Hall problem has continuous translation symmetry, a magnetic unit cell can be introduced as follows: for a torus with primitive vectors $\mathbf{L}_1, \mathbf{L}_2$ enclosing N_ϕ flux quanta, choose two integers $N_1 N_2 = N_\phi$. A lattice is formed by the $N_1 \times N_2$ grid with basis vectors $\mathbf{a}_1 = \mathbf{L}_1 / N_1$ and $\mathbf{a}_2 = \mathbf{L}_2 / N_2$. Since each unit cell encloses one flux quantum, $\mathbf{a}_1 \times \mathbf{a}_2 = 2\pi \ell_B^2$, and hence $t(\mathbf{a}_1)$ and $t(\mathbf{a}_2)$ commute, though their composition has a minus sign,

$$t(\mathbf{a}_1)t(\mathbf{a}_2) = t(\mathbf{a}_2)t(\mathbf{a}_1) = -t(\mathbf{a}_1 + \mathbf{a}_2), \quad 45.$$

a marked distinction from conventional translation symmetry.

We now define Bloch states for the LLL wave functions on the torus in Eq. (42). Since the zeros uniquely determine the LLL wave function, and the magnetic translations $t(\mathbf{a}_i)$ shift the wave function – and therefore the zero pattern – uniformly by \mathbf{a}_i , the zeros of the Bloch states must be arranged on an equally spaced $N_1 \times N_2$ grid on the torus given by

$$\omega_{\mathbf{k}}^{m,n} = a_o(\mathbf{k}) + ma_1 + na_2; \quad m = 0, \dots, N_1 - 1; \quad n = 0, \dots, N_2 - 1, \quad 46.$$

where $a_o(\mathbf{k})$ is the origin of the grid of zeros for the Bloch state at \mathbf{k} . The boundary condition in Eq. 44. fixes the sum of the zeros for every value of \mathbf{k} to be:

$$\sum_{m,n} \omega_{\mathbf{k}}^{m,n} = N_\phi a_o(\mathbf{k}) = \frac{\theta_1}{2\pi} L_2 - \frac{\theta_2}{2\pi} L_1 \pmod{L}, \quad 47.$$

where we have assumed $N_1 = N_2 \pmod{2}$ (there is a small modification otherwise). There are N_ϕ solutions to this equation, given by:

$$a_o(\mathbf{k}) = \frac{\theta_1}{2\pi} \frac{a_2}{N_1} - \frac{\theta_2}{2\pi} \frac{a_1}{N_2} + z_k, \quad z_k = -ik\ell_B^2 \quad 48.$$

where the complexified Bloch momentum is given by

$$k \in \left\{ \frac{i}{\ell_B^2} \left(m \frac{a_2}{N_1} + n \frac{a_1}{N_2} \right) \mid m = 0, \dots, N_1 - 1, n = 0, \dots, N_2 - 1 \right\}. \quad 49.$$

In the complex notation, the reciprocal lattice vectors are given by $b_{1,2} = -ia_{2,1}/\ell_B^2$ so that $\mathbf{a}_i \cdot \mathbf{b}_j = 2\pi\delta_{ij}$; thus Eq. 49. is consistent with the usual notion of momentum on a finite-size torus. The N_ϕ values of k give rise to N_ϕ wave functions (defined momentarily), which span the N_ϕ linearly independent states in the LLL.

The wave functions for the magnetic Bloch states can also be written in terms of a second set of sigma functions, which are quasi-periodic on the torus spanned by $\mathbf{a}_{1,2}$, satisfying

$$\sigma(z + a_i) = -e^{a_i^*(z + \frac{a_i}{2})/\ell_B^2} \sigma(z). \quad 50.$$

This boundary condition is identical to Eq. 43. with $(\mathbf{L}_1, \mathbf{L}_2, N_\phi)$ replaced by $(\mathbf{a}_1, \mathbf{a}_2, 1)$. The magnetic Bloch state wavefunction is then (56),

$$\Phi_{\mathbf{k}}(\mathbf{r}) = \sigma(z - z_k) e^{z_k^* z / \ell_B^2} e^{-\frac{1}{2}|z|^2 / \ell_B^2} e^{-\frac{1}{2}|z_k|^2 / \ell_B^2}, \quad 51.$$

where $z_k = -ik\ell_B^2$. The Gaussian normalization factor $\exp(-\mathbf{k}^2 \ell_B^2 / 2)$ is inserted so that the wavefunction appears symmetric under coordinate and momentum exchange, which will be useful in the next section. From the action of the translation operator in Eq. 38., the magnetic Bloch state $\Phi_{\mathbf{k}}$ transforms as,

$$\hat{t}(\mathbf{a}) \Phi_{\mathbf{k}} = \eta_{\mathbf{a}} e^{i\mathbf{k} \cdot \mathbf{a}} \Phi_{\mathbf{k}}, \quad 52.$$

where the factor $\eta_{\mathbf{a}} = (-1)^{m+n+mn}$ for $\mathbf{a} = m\mathbf{a}_1 + n\mathbf{a}_2$ originates from Eq. 45.. Aside from this phase factor, Eq. 52. resembles Bloch's theorem.

We now return to the inhomogeneous magnetic field, $B(\mathbf{r}) = \bar{B} + \delta B(\mathbf{r})$. Following the discussion in Sec. 3.2, the only effect of a real space modulation of the magnetic field to the wavefunction is a factor $e^{-e\phi(\mathbf{r})/\hbar}$, where the Laplacian of $\phi(\mathbf{r})$ yields the modulation $\delta B(\mathbf{r})$

via Eq. 22.. This establishes a bijective mapping between the Hilbert spaces corresponding to the homogeneous and inhomogeneous fields. If the modulation is periodic on an $N_1 \times N_2$ lattice, the magnetic Bloch momentum \mathbf{k} remains well defined, so that the magnetic Bloch state, which obeys the magnetic translation property in Eq. 52., can be written as

$$\psi_{\mathbf{k}}(\mathbf{r}) = e^{-e\phi(\mathbf{r})/\hbar} e^{-N(\mathbf{k})} \Phi_{\mathbf{k}}(\mathbf{r}), \quad 53.$$

where the term $e^{-N(\mathbf{k})}$ ensures the wave function is normalized. From the resemblance of Eq. 52. to the usual form of Bloch's theorem, Eq. 53. can be regarded as the ‘‘Bloch state’’ of the magnetic translation operator.

3.3.4. Geometry of Bloch states. We now introduce the ‘‘cell periodic part’’ of the magnetic Bloch function $u_{\mathbf{k}}(\mathbf{r}) \equiv e^{-i\mathbf{k}\cdot\mathbf{r}} \psi_{\mathbf{k}}(\mathbf{r})$. Using the definition of z_k in Eq. 48., the Bloch factor $\exp(-i\mathbf{k}\cdot\mathbf{r}) = \exp[-(z_k^* z - z_k z^*)/l_B^2]$. Combined with the wave function in Eq. 53.,

$$u_{\mathbf{k}}(\mathbf{r}) = -e^{-e\phi(\mathbf{r})/\hbar} e^{-N(\mathbf{k})} \Phi_{\mathbf{r}}(\mathbf{k}). \quad 54.$$

Importantly, comparing Eqs. 53. and 54., the \mathbf{r} and \mathbf{k} indices on $\Phi_{\mathbf{r}}(\mathbf{k})$ are exchanged. This reflects a position-momentum duality of the LLL wavefunction: the ‘‘cell periodic function’’ $u_{\mathbf{k}}(\mathbf{r}) \sim \Phi_{\mathbf{r}}(\mathbf{k})$ and the ‘‘Bloch function’’ $\psi_{\mathbf{k}}(\mathbf{r}) \sim \Phi_{\mathbf{k}}(\mathbf{r})$ are related by swapping position and momentum.

Aside from normalization factors, $u_{\mathbf{k}}(\mathbf{r})$ depends only on the holomorphic part of the momentum, z_k . As we will see in Sec. 4, this condition is equivalent to saturating the trace bound in Eq. 8., i.e., $\text{Tr}g_{\mathbf{k}} = \Omega_{\mathbf{k}}$, and is the motivation for the definition of the ideal band.

We now derive the Berry curvature of the Bloch band. To utilize the holomorphic structure of the wave function in momentum space, we introduce the holomorphic $A_{\mathbf{k}} = w_a^* A_{\mathbf{k}}^a$ and anti-holomorphic $\bar{A}_{\mathbf{k}} = w_a A_{\mathbf{k}}^a$ Berry connections. The anti-holomorphic component is easier to compute, as it only depends on the normalization factor,

$$\bar{A}_{\mathbf{k}} \equiv w_a A_{\mathbf{k}}^a = -i\langle u_{\mathbf{k}} | \partial_{\bar{k}} u_{\mathbf{k}} \rangle = i\partial_{\bar{k}} N(\mathbf{k}) + ik\ell_B^2/2, \quad 55.$$

where we have introduced the holomorphic and anti-holomorphic momentum space derivatives, $\partial_k = w_a^* \partial_k^a$ and $\partial_{\bar{k}} = w_a \partial_{\bar{k}}^a$. The holomorphic component of the connection is the complex conjugate of \bar{A} . This gives the Berry curvature (34):

$$\Omega_{\mathbf{k}} = -i\partial_{\bar{k}} \bar{A}_{\mathbf{k}} + i\partial_{\bar{k}} A_{\mathbf{k}} = \ell_B^2 + (\partial_k \partial_{\bar{k}} + \partial_{\bar{k}} \partial_k) N(\mathbf{k}) = \ell_B^2 + \Delta_{\mathbf{k}} N(\mathbf{k}), \quad 56.$$

where $\Delta_{\mathbf{k}} = \partial_k \partial_{\bar{k}} + \partial_{\bar{k}} \partial_k = g_{ab} \partial_k^a \partial_{\bar{k}}^b$ is the Laplacian in momentum space.

That the function $u_{\mathbf{k}}(\mathbf{r})$ is written in the form of a LLL wavefunction on the torus but with the role of position and momentum swapped suggests that ideal bands establish a duality between real and momentum space. This is further supported by the computation of the Berry curvature in Eq. 56., which shows that $\phi(\mathbf{r})$ and $N(\mathbf{k})$ should be viewed as controlling the modulation of the Kähler potentials in real and momentum space, respectively.

3.4. Many-body wavefunctions

We now turn to many-body wave functions built from electrons in the LLL, taking the Laughlin state at filling $\nu = 1/m$ as an example. A crucial feature of a topologically ordered state is its ground state degeneracy, which depends on the genus of the compact manifold on which the problem is studied.

On the infinite plane – which is topologically equivalent to a sphere and thus has a unique ground state – the famous Laughlin wavefunction is written as (57),

$$\Psi_{\text{Laughlin}}(\{z_i\}) = \prod_{i<j} (z_i - z_j)^m \prod_i e^{-\frac{1}{2}|z_i|^2/l_B^2}, \quad 57.$$

where the parameters $z_{i=1,\dots,N_e}$ specify the positions of N_e particles. Comparison to Eq. 18. shows that this many-body wave function is made up entirely of single-particle wave functions in the LLL. The wavefunction also has a special clustering property: when two particles come close, the wavefunction vanishes as their separation to the m^{th} power. This goes beyond the constraints of quantum statistics, which only require linear vanishing for fermions (and none for bosons). The enhanced clustering reflects the structure of the two-particle reduced density matrix and implies that the Laughlin state is the exact ground state of repulsive interactions that penalize pair states with relative angular momentum less than m . This “parent Hamiltonian” can be written as $\sum_{i<j} V(\mathbf{r}_i - \mathbf{r}_j)$, where (58)

$$V(\mathbf{r}) = \sum_{p=0,\dots,m-1} v_p \mathcal{P}_{\text{LLL}} [\nabla^{2p} \delta(\mathbf{r})] \mathcal{P}_{\text{LLL}}, \quad 58.$$

\mathcal{P}_{LLL} denotes the projector into the LLL, and the coefficients $v_p \geq 0$ are related to the Haldane pseudopotentials (59). Only the odd (even) values of p matter for fermions (bosons). Due to the holomorphicity of the LLL, the index p both counts the order of a zero when two particles coincide (clustering) and gives the relative angular momentum of the pair.

The Laughlin wavefunction on the plane generalizes to the torus as:

$$\Psi_{\text{Laughlin}}^{(m)}(\{z_i\}; \boldsymbol{\alpha}) = \prod_{i<j} \tilde{\sigma}^m(z_i - z_j) \prod_{l=1}^m \tilde{\sigma}\left(\sum_i z_i - \alpha_l\right) \prod_i e^{-\frac{1}{2}|z_i|^2/l_B^2}. \quad 59.$$

There are two modifications compared to the wave function on the plane: first, the holomorphic Jastrow factors are replaced by sigma functions, and second, a center of mass term is added. In addition to accounting for the m -fold ground state degeneracy, the latter term ensures that each single particle state in the many-body wave function belongs to the LLL with the correct boundary conditions on the torus, as we now explain.

Following Sec. 3.3.2, to demonstrate that each single particle state belongs to the LLL, it must satisfy two conditions: (1) it has N_ϕ total zeros (counting an order- m zero as m zeros); and (2) the N_ϕ zeros satisfy the boundary condition in Eq. 44.. Now without loss of generality, consider the particle at z_i . The wave function has $(N_e - 1)$ zeros, each of order m , from the Jastrow factors $\tilde{\sigma}^m(z_i - z_j)$ and another m order-one zeros from the center of mass term. Recalling that the Laughlin wave function describes a state at filling $N_e/N_\phi = 1/m$, this does indeed add to N_ϕ total zeros; thus, the first condition is satisfied. To address the second condition requires the sum of the positions of these zeros, $m \sum_{j \neq i} z_j + \sum_l \left(\alpha_l - \sum_{j \neq i} z_j\right) = \sum_l \alpha_l$. There are m linearly independent values of $\boldsymbol{\alpha}$ that satisfy the boundary condition in Eq. 44.. Therefore, the wavefunction is a valid generalization to the torus and there are m linearly independent ground states. Importantly, since the $\tilde{\sigma}(z)$ function is asymptotically equivalent to z for small $|z|$, the Laughlin wavefunction on the torus enjoys identical clustering properties as on the plane.

In an inhomogeneous magnetic field, the generalized Laughlin wave function is identical to Eq. 57. or 59. on the appropriate manifold, with an additional factor $\prod_i e^{-e\phi(\mathbf{r}_i)/\hbar}$. It remains a zero-energy ground state when the interaction term takes the form of Eq. 58., because these additional factors do not modify the clustering property of the FQH states.

4. IDEAL BANDS

Searching for fractionalized phases in models or materials is intrinsically a difficult problem in many-body physics. One approach is to engineer a single-particle band to mimic a Landau level, hoping that fractionalized phases emerge following the paradigm of fractional quantum Hall (FQH) physics. To pursue this approach requires defining what it means for a Bloch band to resemble a Landau level. This section aims to review efforts (32, 22, 30, 33, 34, 35, 36, 37, 38) towards providing “Landau level mimicry criteria” for Bloch bands.

The first challenge is that not all Landau levels are the same: while they share identical topology and Berry curvature, higher Landau levels have a larger quantum metric, i.e., larger $\text{Tr } g$, reflecting that their wavefunctions are more spread out in space. This explains why charge-ordered states are favored in higher Landau levels. The LLL is special as it has the smallest quantum metric and saturates the quantum geometric bound in Eq. 8.. This feature is reflected in its wave function: as discussed in Sec. 3.3.2, the Bloch LLL wave functions are holomorphic in the real-space coordinate z , while their periodic parts $e^{-i\mathbf{k}\cdot\mathbf{r}}\psi_{\mathbf{k}}(\mathbf{r})$ exhibit momentum-space holomorphicity, depending only on k . We will show in this section that these conditions are equivalent: saturating the trace bound is equivalent to the momentum-space holomorphicity of cell-periodic wavefunctions. These special features of the LLL motivate our focus on mimicking it.

Imitating the LLL is not new: Refs. (32, 22, 30) proposed mimicking the famous Girvin-MacDonald-Platzmann (GMP) algebra (60) of density operators in the LLL. There it was shown that the GMP algebra of an isolated Bloch band is satisfied to third order in the momentum of the density operator when the Berry curvature is uniform and the trace bound in Eq. 8. is saturated. Recently it was further proved that the Landau level is the only place where the algebra is exactly satisfied (61).

However, even satisfying the GMP algebra to third order may be too strict: for example, the Aharonov-Casher (45) model describing a $g = 2$ particle in a spatially varying magnetic field (see Sec. 3.2) exhibits an exact zero-energy ground state that generalizes the Laughlin wave function for a short-range interaction. That ground state persists for arbitrarily large variations in magnetic field as long as the interaction remains ideal – for a projected Coulomb interaction, Berry curvature fluctuations will eventually destroy the Laughlin ground state (62). While this model can be far from the limit of uniform Berry curvature, it does saturate the trace bound in Eq. 8.. This further motivates the definition of an *ideal band* as one that saturates the trace bound without imposing any constraint on Berry curvature uniformity. In the following, we review properties of such ideal bands and their wave functions.

4.1. Trace condition and holomorphicity

We define an ideal band as one where the trace bound in Eq. 8., or equivalently, Eq. 9., is saturated for a \mathbf{k} -independent choice of metric, i.e., there exists a \mathbf{k} -independent metric h_{ab} , which defines a complex structure via Eq. 6., such that

$$\text{Tr}_h g_{\mathbf{k}} \equiv h_{ab} g_{\mathbf{k}}^{ab} = |\Omega_{\mathbf{k}}|, \quad \forall \mathbf{k}. \quad 60.$$

We refer to Eq. 60. as saturating the *trace condition*.

A *Kähler band* is defined as one whose cell-periodic part of the Bloch wave function depends on momentum only through its holomorphic component $k = w^a(\mathbf{k})k_a$, up to a normalization factor; it saturates the second inequality (the so-called *determinant bound*)

in Eq. 8..

The following conditions are equivalent:

1. The band $|u_{\mathbf{k}}\rangle$ is an ideal band, saturating the trace condition.
2. The QGT of $|u_{\mathbf{k}}\rangle$ has a \mathbf{k} -independent null vector.
3. The band $|u_{\mathbf{k}}\rangle$ is a Kähler band with \mathbf{k} -independent complex structure.

More concisely, an ideal band can be written as,

$$|u_{\mathbf{k}}\rangle = \frac{1}{\mathcal{N}_{\mathbf{k}}} |\tilde{u}_{\mathbf{k}}\rangle, \quad 61.$$

where $|u_{\mathbf{k}}\rangle$ denotes the normalized cell-periodic part of the Bloch wave function, $\mathcal{N}_{\mathbf{k}}$ is a real normalization factor, and $|\tilde{u}_{\mathbf{k}}\rangle$ depends on the momentum only through the holomorphic component of the momentum coordinate, so that $\partial_{\bar{k}}|\tilde{u}_{\mathbf{k}}\rangle = 0$.

The equivalence of conditions 1. and 2. is reviewed in the SM Sec. 7.1. That holomorphicity (condition 3) implies the trace bound (conditions 1, 2) was noticed in early literature such as Ref. (63). We provide a quick proof following Ref. (33). The starting point is to rewrite the QGT in terms of the unnormalized state $|\tilde{u}_{\mathbf{k}}\rangle$ as

$$Q_{\mathbf{k}}^{ab} = \frac{\langle \partial_{\bar{k}}^a \tilde{u}_{\mathbf{k}} | \partial_{\bar{k}}^b \tilde{u}_{\mathbf{k}} \rangle}{\mathcal{N}_{\mathbf{k}}^2} - \frac{\langle \partial_{\bar{k}}^a \tilde{u}_{\mathbf{k}} | \tilde{u}_{\mathbf{k}} \rangle \langle \tilde{u}_{\mathbf{k}} | \partial_{\bar{k}}^b \tilde{u}_{\mathbf{k}} \rangle}{\mathcal{N}_{\mathbf{k}}^4}. \quad 62.$$

By virtue of being a holomorphic band, $\partial_{\bar{k}}|\tilde{u}_{\mathbf{k}}\rangle = 0$ (recall $\partial_{\bar{k}} = w_b \partial_k^b$). Thus, Eq. 62. implies $Q_{\mathbf{k}}^{ab} w_b = 0$, so that the QGT has a constant null vector.

In the other direction, that saturating the quantum geometrical bound implies the holomorphicity of Bloch states was proved in Ref. (35, 36) by showing that a Bloch state, formally regarded as a mapping from the BZ torus to complex projective space, is a holomorphic immersion if and only if the determinant bound (second inequality in Eq. 8.) is saturated, motivating the definition of the Kähler band above. An ideal band is a special class of Kähler band whose complex structure is constant across the BZ. Quasi-Kähler bands are Kähler bands where the Berry curvature vanishes at at least one momentum, which is the case for two-band models in 2D (35).

Vortexability provides a real-space perspective on ideal bands and beyond (37). Defining \mathcal{P} as the band projector and $1 - \mathcal{P}$ as its complement, the vortexability criterion states that there exists a vortex operator $z(\mathbf{r})$ associated with every point in real space such that $(1 - \mathcal{P})z(\mathbf{r})\mathcal{P} = 0$. In an ideal band, the vortex operator is simply the holomorphic component of the position operator $z = w_a r^a$, and vortexability illustrates the real-space holomorphic properties of ideal bands. Such a real-space perspective enables the direct construction of exact FCI ground states for ideal bands with short-range interactions (37, 64); see Sec. 4.3. Vortexability also implies perfect circular magnetic dichroism in optical responses (65).

A comparison of Kähler, ideal and vortexable bands is summarized in Fig. 1. The LLL is the classic example of an ideal band. More examples and their experimental relevance are discussed in Sec. 4.4. In the SM Sec. 7.3 we provide an example of a vortexable but non-ideal band.

4.2. From holomorphicity to ideal band wavefunctions

We now seek an explicit form of the wave function of an ideal band. As discussed in Sec. 2.1, a non-zero Chern number implies the absence of a globally defined smooth gauge choice for

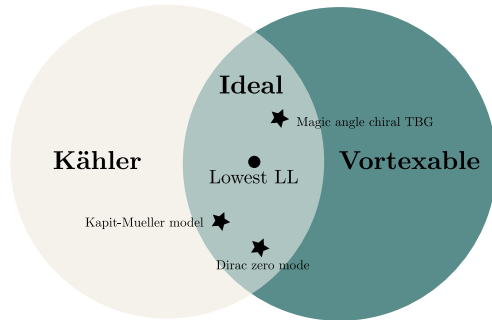


Figure 1

The relationship between Kähler, ideal, and vortexable bands. Kähler and vortexable bands are defined by momentum and real space holomorphicity, respectively, while ideal bands lie at their intersection. Figure adopted from Ref. (66).

Bloch wave functions. In the following we assume a gauge that is smooth inside of the BZ torus, which implies a discontinuity at the BZ boundary.

As discussed in the previous section, the trace condition *necessarily* and *sufficiently* ensures the holomorphicity of the Bloch state, i.e., the state can be written in the form of Eq. 61.. As we learned from the LLL wavefunction that real space holomorphicity strongly constrains the real space wavefunction (see Sec. 3.3.2), similarly, momentum space holomorphicity strongly constrains the analytical form of ideal band Bloch wavefunctions.

To understand the constraint, we start by comparing the periodic functions at momenta related by reciprocal lattice vectors. The states must obey,

$$\tilde{u}_{k+b_i}(\mathbf{r}) = e^{i\theta_i(\mathbf{r})} e^{i\phi_i(k)} \tilde{u}_k(\mathbf{r}), \quad \theta_i \equiv -\mathbf{b}^i \cdot \mathbf{r}, \quad 63.$$

where we have used b^i to denote the complex reciprocal lattice vector. The condition parallels the boundary condition on the holomorphic part of the LLL wave function on the torus in Eq. 40.: the phase $\phi_i(k)$ is required to be holomorphic and the phase $\exp(-i\mathbf{b}_i \cdot \mathbf{r})$ is dual to the fictitious flux appearing in Eq. 40.. Mathematically, the analog to the contour integral in Eq. 41. arises because for any real space point \mathbf{r} , the Chern number reflects the boundary integral of \tilde{u}_k under a smooth choice of gauge, yielding

$$C = \frac{1}{2\pi i} \oint dk \partial_k \ln \tilde{u}_k(\mathbf{r}). \quad 64.$$

This suggests that in an ideal band $\tilde{u}_k(\mathbf{r})$, one should view coordinate \mathbf{r} as tuning the ‘fictitious flux’ determining the dual boundary condition, parallel to (θ_1, θ_2) in the quantum Hall problem, and one should regard the Chern number C as the ‘total flux quanta’, parallel to N_ϕ in the quantum Hall problem (67). This comparison can be made exact. The model calculations in Fig. 2 show the wave function of an ideal band, which indeed has C zeros when plotted in \mathbf{k} -space for fixed \mathbf{r} . The C zeros must sum to the real space coordinate \mathbf{r} , paralleling the constraint on the sum of zeros in Eq. 44..

The ideal band wave function can be obtained in the same spirit as the quantum Hall wave function on the torus: holomorphicity ensures that once a wave function is found, it is unique. In the $C = 1$ case, the ideal band wavefunction must take the form (34),

$$\psi_{\mathbf{k}}(\mathbf{r}) = e^{-N(k)} \mathcal{B}(\mathbf{r}) \Phi_{\mathbf{k}}(\mathbf{r}), \quad 65.$$

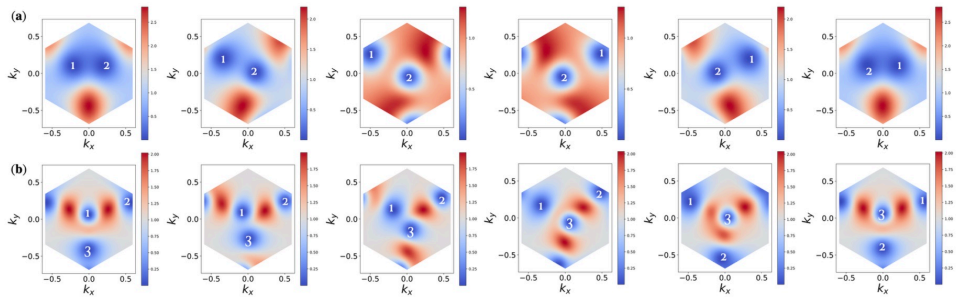


Figure 2

Cell-periodic part of the Bloch wave function of an ideal band with Chern number $C = 2$ in panel (a) and Chern number $C = 3$ in panel (b). Each column is a plot of $|u_{\mathbf{k}}(\mathbf{r})|$ as a function of \mathbf{k} for different choices of \mathbf{r} , sampled linearly on a line from the initial point \mathbf{r}_0 to the final point $\mathbf{r}_0 + \mathbf{a}$, where \mathbf{a} is a lattice vector. The center of the \mathbf{k} -space zeros are evolving linearly in the BZ following the change of \mathbf{r} . Figure adopted from Ref. (67).

where $N(\mathbf{k})$ is the normalization factor that accounts for the variation of Berry curvature in momentum space, and $\mathcal{B}(\mathbf{r})$ is a momentum independent factor. The wave function in Eq. 65. is quite similar to the Aharonov-Casher wavefunction discussed in Eq. 53., except with the exponential of the scalar field $\exp[-e\phi(\mathbf{r})/\hbar]$ in Eq. 53. replaced by $\mathcal{B}(\mathbf{r})$. Notice that the wave function in Eq. 65. is still a Bloch wave function, which obeys the standard translation properties of Bloch bands, in contrast to the magnetic translation properties of states in the LLL. Thus, the factor $\mathcal{B}(\mathbf{r})$ must be quasi-periodic in the real space to compensate for the quasi-periodicity of the LLL wavefunction $\Phi_{\mathbf{k}}(\mathbf{r})$.

For a more general $C > 1$ ideal band, the wavefunction is given by (67, 64),

$$\psi_{\mathbf{k}}(\mathbf{r}) = e^{-N(\mathbf{k})} \sum_{\sigma=1}^C \mathcal{B}(\mathbf{r} + \sigma \mathbf{a}_1) \Phi_{\mathbf{k}}(\mathbf{r} + \sigma \mathbf{a}_1). \quad 66.$$

The ideal band has also been generalized to higher Landau levels and applied to fractionalization in moiré systems (66, 68, 69, 70).

4.3. Implication of ideal bands for fractional Chern insulators

An important property of ideal bands is that model FCI wave functions are exact zero energy ground states at the appropriate filling and with short ranged interactions. Here we focus on $C = 1$, but the statement extends to ideal bands with $C > 1$ (67, 64).

For a $C = 1$ ideal band, the ideal quantum geometry implies an isomorphism to the LLL states, as shown by Eqs. 65. and 53.. Hence, the many-body wave functions are also in one-to-one correspondence. Thus, a many-body quantum Hall wave function in the LLL, immediately yields a corresponding generalized FCI wave function in a particular ideal band. For instance, the generalized $\nu = 1/m$ Laughlin state in an ideal band is,

$$\Psi_{\text{ideal}}^{(m)}(\{z_i\}, \boldsymbol{\alpha}) = \left[\prod_i \mathcal{B}(\mathbf{r}_i) \right] \Psi_{\text{Laughlin}}^{(m)}(\{z_i\}, \boldsymbol{\alpha}), \quad 67.$$

where $\Psi_{\text{Laughlin}}^{(m)}(\{z_i\}, \boldsymbol{\alpha})$ is the LLL Laughlin wave function in Eq. 59.. From the wave function in Eq. 65., $\Psi_{\text{ideal}}^{(m)}$ is within the Fock space determined by the ideal band. Additionally,

from the form of the Laughlin wave function, as $z = z_i - z_j \rightarrow 0$, the wave function vanishes as z^m and thus the probability density vanishes as $|z|^{2m}$. Hence, following Ref. (33, 37), the interaction energy of $\Psi_{\text{Laughlin}}^{(m)}$ vanishes for any two-body interaction term of the form of Eq. 58..

4.4. Examples of ideal bands and experimental relevance

So far, we have provided two examples of ideal bands: the LLL ($n = 0$) and the Aharonov-Casher band. While individual higher $n \geq 1$ Landau levels are not ideal, the many-body state formed by filling the lowest $p \geq 0$ Landau levels together yield an ideal band. This essential fact enables the generalization of ideal bands to higher Landau levels (66, 68).

Beyond Landau levels and Aharonov-Casher model, ideal bands are now realized in many lattice systems. In particular, ideal bands have attracted significant attention due to their relevance to twisted bilayer graphene: in the “chiral model” of twisted bilayer graphene (71) at the magic twist angle, the system exhibits two exactly flat bands, each localized on a different sublattice and each realizing an ideal band with Chern number $C = 1$. As a result, exact fractional Chern insulator states are theoretically predicted in this limit (33). Although in realistic twisted bilayer graphene systems, stabilizing fractionalized phases typically requires a finite magnetic field (72), the exact results in the chiral limit provide important insights into the emergence of fractionalized phases in twisted materials.

The first zero field FCI was observed in moiré MoTe_2 (24, 25, 26, 27). Theoretical calculations based on both first principle and continuum models indicate that the narrow band in such systems resembles a LLL in many aspects, including the nearly uniform Berry curvature distribution, near-ideal quantum geometry and narrow band dispersions (73, 74, 75, 76, 77, 78, 79, 80). Later theoretical work proposed that the origin of such LLL-like flat bands arises from real-space skyrmion winding: the spatial winding of the layer pseudospin generates an effective magnetic field experienced by electrons that follow this texture (81). This provides an intuitive explanation for the emergence of nearly ideal bands in twisted MoTe_2 within the Aharonov-Casher framework (82).

The second zero field FCI was observed in rhombohedral graphene with aligned hexagonal boron nitride (28, 29), for which ideal band models have also been developed (83, 84).

Beyond twisted materials, ideal bands or near-ideal bands are predicted in periodically strained (85, 86) and nano-patterned materials (87, 88, 89).

Finally, ideal bands can be realized in tight-binding models. A notable example is the Kapit-Mueller model (90), where the hopping parameters are carefully engineered to achieve a positive semi-definite spectrum with an exactly flat band. Remarkably, the wavefunctions of this flat band take the form of lattice analogs of LLL states. In this sense, the Kapit-Mueller model provides a tight-binding realization of an ideal band, distinguishing it from continuum constructions such as the Aharonov-Casher approach or moiré-based systems described above. We briefly review this model in the SM Sec. 7.3.

5. BEYOND IDEAL BANDS

5.1. Deviations from ideality

Given the importance of ideal bands for FCIs, it is desirable to develop criteria to measure the deviations from ideal bands. To this end, two geometric indicators have been most

commonly studied: the first is standard deviation of the Berry curvature:

$$F = \left[\int_{\text{BZ}} \frac{d^2 \mathbf{k}}{A_{\text{BZ}}} \left(C - \Omega_{\mathbf{k}} \frac{A_{\text{BZ}}}{2\pi} \right)^2 \right]^{1/2}, \quad 68.$$

which was first introduced in the context of mimicking the GMP algebra (32) (see Sec. 4). The second indicator is the deviation from the ideal band condition:

$$\bar{T} = \min_{\omega} \int_{\text{BZ}} \frac{d^2 \mathbf{k}}{A_{\text{BZ}}} (\text{Tr}_{\omega} g_{\mathbf{k}} - |\Omega_{\mathbf{k}}|), \quad 69.$$

i.e., the deviation from the ideal band condition minimized over all choices of the matrix ω , which was introduced in Ref. (77), motivated by Refs. (30, 31). The bounds in Eq. 8. imply that $\bar{T} \geq 0$.

Minimizing F and \bar{T} has been shown to be correlated with the stability of an FCI ground state (31, 91, 92, 77, 93). However, these single-particle properties are not sufficient to determine the existence of an FCI: the many-body ground state fundamentally depends on the details of the interactions. The motivation for considering such indicators is that an FCI in an ideal band represents a special point within a broader topological phase that can persist under small deformations of the Hamiltonian. Yet, even in an ideal band, the model FCI wave function discussed in Sec. 4.3 is an exact ground state only for the short-range interactions specified in Eq. 58.. Indeed, modifying the interaction range (94) or introducing Berry curvature fluctuations (62), even while keeping the band geometry fixed, can destabilize the FCI ground state.

5.2. Orbital embedding

A further limitation of the deviations introduced in Sec. 5.1 arises because the QGT is not invariant under the choice of orbital embedding, as mentioned in Sec. 2.2.2. (See Ref. (40) for a detailed and pedagogical discussion.) Thus, despite their success, the geometrical indicators described in Sec. 5.1 cannot alone be reliable indicators of an FCI ground state, which again reflects the fundamental fact that a many-body ground state cannot be fully determined from single-particle physics alone. In the SM Sec. 7.3, we demonstrate the importance of embedding dependence in the Kapit–Mueller model by numerically studying the effect of embedding variations on the exact Laughlin $\nu = 1/2$ state stabilized by on-site repulsion. We find that changing the embedding destroys the single-particle ideal band condition, while leaving both the single-particle band structure and the many-body spectrum unchanged. Ultimately, the embedding change converts an ideal flat band into a vortexable non-ideal flat band, underscoring the sensitivity of band geometry to the embedding despite the invariance of the spectrum.

5.3. Fractional Chern insulators far from the lowest Landau level

We briefly mention the important observation that FCIs can exist in bands far from the LLL or ideal band limit (95, 96), including in bands with vanishing Chern number (97, 98, 99, 100). Whether an analog of ideal bands exists for these cases remains an open question.

6. OUTLOOK

The developments reviewed here point toward a unifying perspective in which quantum geometry plays a central role in organizing and stabilizing fractional topological phases in Bloch bands. In particular, the emergence of momentum-space holomorphicity and the saturation of geometric bounds suggest that a class of Bloch bands can faithfully emulate the Hilbert space structure of Landau levels, providing a promising route toward realizing fractionalized phases in vanishing magnetic field.

Several open questions remain. A key challenge is to establish robust and broadly applicable criteria that relate geometric properties of Bloch bands to the stability of interacting phases. While the trace condition and related bounds offer valuable guidance, their precise role in realistic systems, where band dispersion, disorder, and multiband effects are unavoidable, remains to be fully understood. Extending these ideas beyond idealized limits, and clarifying the extent to which the holomorphic structure can persist or be approximated in experimentally relevant settings, is an important direction for future work. On the experimental front, rapidly advancing platforms such as moiré materials provide unprecedented opportunities to engineer and probe quantum geometry in situ. The ability to tune band structure, interactions, and symmetry suggests that geometric optimization may become a practical design principle for stabilizing fractionalized phases. In this context, developing direct probes of the quantum metric and its interplay with Berry curvature will be crucial for connecting theoretical criteria to observable signatures. More broadly, the interplay between geometry, topology, and interactions continues to reveal new structures beyond those rooted in Landau levels. Understanding how these elements combine to produce robust many-body phases – potentially in settings without direct analogues in continuum quantum Hall systems – remains an exciting frontier.

DISCLOSURE STATEMENT

The authors are not aware of any affiliations, memberships, funding, or financial holdings that might be perceived as affecting the objectivity of this review.

ACKNOWLEDGMENTS

The authors are grateful for fruitful conversations and collaborations with Dathan Ault-McCoy, Lei Chen, Valentin Crépel, Junkai Dong, Nicolás Morales-Durán, Liang Fu, Daniele Guerci, Duncan Haldane, Guangyue Ji, Eslam Khalaf, Semyon Klevtsov, Patrick Ledwith, Nabil Lhachemi, Zhao Liu, Bruno Mera, Andrew Millis, Tomoki Ozawa, David Palomino, Daniel Parker, Xin Shen, Kai Sun, Ashvin Vishwanath, Fengcheng Wu, Di Xiao, Bo Yang, Kang Yang and Wang Yao. The authors are especially grateful to Nabil Lhachemi, Zhao Liu and Tomoki Ozawa for their feedback on this manuscript and to Jinjie Zhang for producing Supplemental Fig. 1. J.C. acknowledges support from the Flatiron Institute, a division of the Simons Foundation.

LITERATURE CITED

1. Xiao D, Chang MC, Niu Q. 2010. *Rev. Mod. Phys.* 82(3):1959–2007
2. Törmä P. 2023. *Phys. Rev. Lett.* 131(24):240001

3. Yu J, Bernevig BA, Queiroz R, Rossi E, Törmä P, Yang BJ. 2025. *npj Quantum Materials* 10(1):101
4. Jiang Y, Holder T, Yan B. 2025. *Reports on Progress in Physics* 88(7):076502
5. Gao A, Nagaosa N, Ni N, Xu SY. 2025. *Preprint arXiv:2508.00469*
6. King-Smith RD, Vanderbilt D. 1993. *Phys. Rev. B* 47(3):1651–1654
7. Resta R. 1994. *Rev. Mod. Phys.* 66(3):899–915
8. Sundaram G, Niu Q. 1999. *Phys. Rev. B* 59(23):14915–14925
9. Haldane FDM. 2004. *Phys. Rev. Lett.* 93(20):206602
10. Marzari N, Mostofi AA, Yates JR, Souza I, Vanderbilt D. 2012. *Rev. Mod. Phys.* 84(4):1419–1475
11. Niu Q, Thouless DJ, Wu YS. 1985. *Phys. Rev. B* 31(6):3372–3377
12. Souza I, Wilkens T, Martin RM. 2000. *Phys. Rev. B* 62(3):1666–1683
13. Haldane FDM. 2011. *Phys. Rev. Lett.* 107(11):116801
14. Liang J, Liu Z, Yang Z, Huang Y, Wurstbauer U, et al. 2024. *Nature* 628(8006):78–83
15. Can T, Laskin M, Wiegmann PB. 2015. *Annals of Physics* 362:752–794
16. Andrei EY, Efetov DK, Jarillo-Herrero P, MacDonald AH, Mak KF, et al. 2021. *Nat. Rev. Mater.* 6(3):201–206
17. Nuckolls KP, Yazdani A. 2024. *Nat. Rev. Mater.* 9(7):460–480
18. Cao T, Fu L, Ju L, Xiao D, Xu X. 2026. *Annu. Rev. of Condens. Matter. Phys.* 17(Volume 17, 2026):233–256
19. Regnault N, Bernevig BA. 2011. *Phys. Rev. X* 1(2):021014
20. Sheng D, Gu ZC, Sun K, Sheng L. 2011. *Nat. Comm.* 2(1):389
21. Neupert T, Santos L, Chamon C, Mudry C. 2011. *Phys. Rev. Lett.* 106(23):236804
22. Parameswaran SA, Roy R, Sondhi SL. 2013. *Comptes Rendus Physique* 14(9-10):816–839
23. Liu Z, Bergholtz EJ. 2022. *arXiv e-prints* :arXiv:2208.08449
24. Cai J, Anderson E, Wang C, Zhang X, Liu X, et al. 2023. *Nature* 622(7981):63–68
25. Zeng Y, Xia Z, Kang K, Zhu J, Knüppel P, et al. 2023. *Nature* 622(7981):69–73
26. Park H, Cai J, Anderson E, Zhang Y, Zhu J, et al. 2023. *Nature* 622(7981):74–79
27. Xu F, Sun Z, Jia T, Liu C, Xu C, et al. 2023. *Phys. Rev. X* 13(3):031037
28. Lu Z, Han T, Yao Y, Reddy AP, Yang J, et al. 2024. *Nature* 626(8000):759–764
29. Xie J, Huo Z, Lu X, Feng Z, Zhang Z, et al. 2025. *Nature Materials* 24(7):1042–1048
30. Roy R. 2014. *Phys. Rev. B* 90(16):165139
31. Jackson TS, Möller G, Roy R. 2015. *Nat. Comm.* 6(1):8629
32. Parameswaran S, Roy R, Sondhi SL. 2012. *Phys. Rev. B* 85(24):241308
33. Ledwith PJ, Tarnopolsky G, Khalaf E, Vishwanath A. 2020. *Phys. Rev. Res.* 2(2):023237
34. Wang J, Cano J, Millis AJ, Liu Z, Yang B. 2021. *Phys. Rev. Lett.* 127(24):246403
35. Mera B, Ozawa T. 2021. *Phys. Rev. B* 104(4):045104
36. Ozawa T, Mera B. 2021. *Phys. Rev. B* 104(4):045103
37. Ledwith PJ, Vishwanath A, Parker DE. 2023. *Phys. Rev. B* 108(20):205144
38. Estienne B, Regnault N, Crépel V. 2023. *Phys. Rev. Res.* 5(3):L032048
39. Dobardžić E, Dimitrijević M, Milovanović M. 2014. *Phys. Rev. B* 89(23):235424
40. Simon SH, Rudner MS. 2020. *Phys. Rev. B* 102(16):165148
41. Macdonald AH. 1994. *Preprint cond-mat/9410047*
42. Girvin SM. 1999. *Preprint cond-mat/9907002*
43. Tong D. 2016. *Preprint arXiv:1606.06687*
44. Arovas D. 2024. Lecture notes on quantum hall effect (a work in progress). <https://courses.physics.ucsd.edu/2019/Spring/physics230/LECTURES/QHE.pdf>
45. Aharonov Y, Casher A. 1979. *Phys. Rev. A* 19(6):2461–2462
46. Dong J, Wang J, Fu L. 2022. *arXiv e-prints* :arXiv:2208.10516
47. Novoselov KS, Geim AK, Morozov SV, Jiang D, Katsnelson MI, et al. 2005. *Nature* 438(7065):197–200

48. Zhang Y, Tan YW, Stormer HL, Kim P. 2005. *Nature* 438(7065):201–204
49. Gusynin V, Sharapov S. 2005. *Phys. Rev. Lett.* 95(14):146801
50. Peres N, Guinea F, Castro Neto A. 2006. *Phys. Rev. B* 73(12):125411
51. Haldane FDM, Rezayi EH. 1985. *Phys. Rev. B* 31(4):2529–2531
52. Haldane FDM. 1985. *Phys. Rev. Lett.* 55(20):2095–2098
53. Haldane FDM. 2018. *Journal of Mathematical Physics* 59(7):071901
54. Wang J, Geraedts SD, Rezayi EH, Haldane FDM. 2019. *Phys. Rev. B* 99(12):125123
55. Haldane F. 2018. *Journal of Mathematical Physics* 59(7)
56. Wang J, Zheng Y, Millis AJ, Cano J. 2021. *Phys. Rev. Res.* 3(2):023155
57. Laughlin RB. 1983. *Phys. Rev. Lett.* 50(18):1395
58. Trugman SA, Kivelson S. 1985. *Phys. Rev. B* 31(8):5280
59. Haldane FDM. 1983. *Phys. Rev. Lett.* 51(7):605–608
60. Girvin S, MacDonald A, Platzman P. 1986. *Phys. Rev. B* 33(4):2481
61. Wang Z, Simon SH. 2025. *Phys. Rev. Lett.* 134(13):136502
62. Shi J, Cano J, Morales-Durán N. 2025. *Preprint arXiv:2503.15900*
63. Claassen M, Lee CH, Thomale R, Qi XL, Devereaux TP. 2015. *Phys. Rev. Lett.* 114(23):236802
64. Dong J, Ledwith PJ, Khalaf E, Lee JY, Vishwanath A. 2023. *Phys. Rev. Res.* 5(2):023166
65. Dong J, Wang J, Ledwith PJ, Vishwanath A, Parker DE. 2023. *Phys. Rev. Lett.* 131(13):136502
66. Liu Z, Mera B, Fujimoto M, Ozawa T, Wang J. 2025. *Phys. Rev. X* 15(3):031019
67. Wang J, Klevtsov S, Liu Z. 2023. *Phys. Rev. Res.* 5(2):023167
68. Fujimoto M, Parker DE, Dong J, Khalaf E, Vishwanath A, Ledwith P. 2025. *Phys. Rev. Lett.* 134(10):106502
69. Li B, Wu F. 2025. *Phys. Rev. B* 111(12):125122
70. Li B, Ouyang Y, Wu F. 2026. *arXiv e-prints* :arXiv:2601.13169
71. Tarnopolsky G, Kruchkov AJ, Vishwanath A. 2019. *Phys. Rev. Lett.* 122(10):106405
72. Xie Y, Pierce AT, Park JM, Parker DE, Khalaf E, et al. 2021. *Nature* 600(7889):439–443
73. Wu F, Lovorn T, Tutuc E, Martin I, MacDonald AH. 2019. *Phys. Rev. Lett.* 122(8):086402
74. Devakul T, Crépel V, Zhang Y, Fu L. 2021. *Nat. Comm.* 12(1):6730
75. Li H, Kumar U, Sun K, Lin SZ. 2021. *Phys. Rev. Res.* 3(3):L032070
76. Crépel V, Fu L. 2023. *Phys. Rev. B* 107(20):L201109
77. Morales-Durán N, Wang J, Schleder GR, Angeli M, Zhu Z, et al. 2023. *Phys. Rev. Res.* 5(3):L032022
78. Jia Y, Yu J, Liu J, Herzog-Arbeitman J, Qi Z, et al. 2024. *Phys. Rev. B* 109(20):205121
79. Crépel V, Regnault N, Queiroz R. 2024. *Comm. Phys.* 7(1):146
80. Wang C, Zhang XW, Liu X, Wang J, Cao T, Xiao D. 2025. *Phys. Rev. Lett.* 134(7):076503
81. Morales-Durán N, Wei N, Shi J, MacDonald AH. 2024. *Phys. Rev. Lett.* 132(9):096602
82. Shi J, Morales-Durán N, Khalaf E, MacDonald AH. 2024. *Phys. Rev. B* 110(3):035130
83. Bernevig BA, Kwan YH. 2025. *Preprint arXiv:2503.09692*
84. Tan T, Ledwith PJ, Devakul T. 2025. *Preprint arXiv:2511.07402*
85. Gao Q, Dong J, Ledwith P, Parker D, Khalaf E. 2023. *Phys. Rev. Lett.* 131(9):096401
86. Wan X, Sarkar S, Lin SZ, Sun K. 2023. *Phys. Rev. Lett.* 130(21):216401
87. Ghorashi SAA, Dunbrack A, Abouelkomsan A, Sun J, Du X, Cano J. 2023. *Phys. Rev. Lett.* 130(19):196201
88. Zeng Y, Wolf TM, Huang C, Wei N, Ghorashi SAA, et al. 2024. *Phys. Rev. B* 109(19):195406
89. Ault-McCoy D, Lhachemi MNY, Dunbrack A, Ghorashi SAA, Cano J. 2026. *Phys. Rev. B* 113(7):075140
90. Kapit E, Mueller E. 2010. *Phys. Rev. Lett.* 105(21):215303
91. Bauer D, Jackson T, Roy R. 2016. *Phys. Rev. B* 93(23):235133
92. Parker D, Ledwith P, Khalaf E, Soejima T, Hauschild J, et al. 2021. *Preprint arXiv:2112.13837*
93. Wu AK, Sarkar S, Wan X, Sun K, Lin SZ. 2024. *Phys. Rev. Res.* 6(3):L032063
94. Emanuel P, Keselman A, Oreg Y. 2025. *Phys. Rev. B* 112(23):235133

95. Bauer D, Talkington S, Harper F, Andrews B, Roy R. 2022. *Phys. Rev. B* 105(4):045144
96. Andrews B, Raja M, Mishra N, Zaletel MP, Roy R. 2024. *Phys. Rev. B* 109(24):245111
97. Simon SH, Harper F, Read N. 2015. *Phys. Rev. B* 92(19):195104
98. Kourtis S. 2018. *Phys. Rev. B* 97(8):085108
99. Lin Z, Lu H, Yang W, Zhai D, Yao W. 2025. *Preprint arXiv:2505.09009*
100. Liu H, Perea-Causin R, Liu Z, Bergholtz EJ. 2025. *Preprint arXiv:2510.15027*
101. Zhang Y, Sarkar S, Wan X, Parker DE, Lin SZ, Sun K. 2025. *Preprint arXiv:2510.22831*

7. SUPPLEMENTAL MATERIAL

7.1. Geometric bound and null vectors

In this section we derive the bounds on the QGT and their relation to its null vectors.

The QGT is defined as

$$Q_{\mathbf{k}}^{ab} = g_{\mathbf{k}}^{ab} + \frac{i\epsilon^{ab}}{2}\Omega_{\mathbf{k}}. \quad 70.$$

Since it is Hermitian and non-negative, it has two real and non-negative eigenvalues, $\lambda_{1,2}(\mathbf{k})$, and its determinant must be non-negative. This yields:

$$\begin{aligned} 0 \leq 2 \det Q_{\mathbf{k}} &= \epsilon_{ac}\epsilon_{bd} \left(g_{\mathbf{k}}^{ab} + \frac{i\epsilon^{ab}}{2}\Omega_{\mathbf{k}} \right) \left(g_{\mathbf{k}}^{cd} + \frac{i\epsilon^{cd}}{2}\Omega_{\mathbf{k}} \right) \\ &= \epsilon_{ac}\epsilon_{bd} g_{\mathbf{k}}^{ab} g_{\mathbf{k}}^{cd} - \frac{1}{4} \epsilon_{ac}\epsilon_{bd} \epsilon^{ab} \epsilon^{cd} |\Omega_{\mathbf{k}}|^2 = 2 \det g_{\mathbf{k}} - \frac{1}{2} |\Omega_{\mathbf{k}}|^2, \end{aligned} \quad 71.$$

which yields the determinant bound $\sqrt{\det g_{\mathbf{k}}} \geq |\Omega_{\mathbf{k}}|/2$. The inequality saturates if and only if one of $\lambda_{1,2}(\mathbf{k})$ is zero; otherwise $\det Q_{\mathbf{k}}$ is strictly positive. Thus, saturation of the determinant bound implies that $Q_{\mathbf{k}}^{ab}$ has a null vector. In general, the null vector can be \mathbf{k} -dependent – in fact, every two-band model in 2D saturates the determinant bound at every \mathbf{k} with a \mathbf{k} -dependent null vector (35).

Using the inequality of arithmetic and geometric means, the trace of a 2×2 non-negative Hermitian matrix is lower bounded by twice the square root of its determinant, yielding the following quantum geometric bound,

$$\text{Tr}_h g_{\mathbf{k}} \geq 2\sqrt{\det g_{\mathbf{k}}} \geq |\Omega_{\mathbf{k}}|, \quad 72.$$

for any positive symmetric matrix h_{ab} with $\det h = 1$.

We now show that saturation of both bounds with a \mathbf{k} -independent matrix h – i.e., satisfying the ideal band condition – implies that the QGT has a \mathbf{k} -independent null vector. To this end, we rewrite h in terms of complex vectors w, w^* as

$$h_{ab} = w_a^* w_b + w_a w_b^*, \quad i\epsilon_{ab} = w_a^* w_b - w_a w_b^*. \quad 73.$$

The non-negativity of the QGT implies

$$0 \leq w_a^* Q_{\mathbf{k}}^{ab} w_b = \frac{1}{2} [h_{ab} + i\epsilon_{ab}] \left(g_{\mathbf{k}}^{ab} + \frac{i\epsilon^{ab}}{2}\Omega_{\mathbf{k}} \right) = \frac{1}{2} \left(h_{ab} g_{\mathbf{k}}^{ab} - \Omega_{\mathbf{k}} \right). \quad 74.$$

Saturation of both bounds in Eq. 72. implies that the right-hand-side of Eq. 74. vanishes, which then implies that w is a (\mathbf{k} -independent) null vector of $Q_{\mathbf{k}}$.

Thus, the ideal band condition is much stronger than the determinant condition: it is a global trace bound that requires the null vector of the QGT be momentum-independent.

7.2. Translation operator in the lowest Landau level

In this section, we derive how the translation operator acts on wave functions in the LLL. Starting from the definition of the translation operator,

$$t(\mathbf{d}) = \exp(i\mathbf{d} \times \mathbf{R}/\ell_B^2) = \exp \left[(d^* \hat{b}^\dagger - d \hat{b})/\ell_B \right], \quad 75.$$

we expand it using the Baker-Campbell-Hausdorff relation $e^{A+B} = e^A e^B e^{-\frac{1}{2}[A,B]}$ as:

$$t(\mathbf{d}) = e^{d^* \hat{b}^\dagger - d \hat{b}} = e^{-\frac{1}{2}|d|^2} e^{d^* \hat{b}^\dagger} e^{-d \hat{b}} = e^{-\frac{1}{2}|d|^2} e^{d^* (-\bar{\partial} + z/2)} e^{-d(\partial + \bar{z}/2)}, \quad 76.$$

where we have set $\ell_B = 1$ and in the last equality used the explicit form of the raising and lowering operators,

$$\hat{b} = \partial_z + \frac{\bar{z}}{2}, \quad \hat{b}^\dagger = -\partial_{\bar{z}} + \frac{z}{2}. \quad 77.$$

To act with this operator on a wave function, recall the more familiar translation operator $e^{d\partial_z} f(z) = f(z+d)$, which can be derived quite generally using the Taylor expansion for a single-variable function,

$$f(z+d) = f(z) + d\partial_z f(z) + \frac{1}{2!} d^2 \partial_z^2 f(z) + \dots = e^{d\partial_z} f(z). \quad 78.$$

Acting on a LLL wave function yields:

$$e^{-d(\partial + \bar{z}/2)} f(z) e^{-\frac{1}{2}|z|^2} = f(z-d) e^{-\frac{1}{2}|z|^2} \quad 79.$$

and ultimately

$$t(\mathbf{d}) f(z) e^{-\frac{1}{2}|z|^2} = e^{-\frac{1}{2}|d|^2} e^{z d^*} f(z-d) e^{-\frac{1}{2}|z|^2}, \quad 80.$$

which can be rewritten as,

$$t(\mathbf{d}) \psi_{\text{LLL}}(\mathbf{r}) = \psi_{\text{LLL}}(\mathbf{r} - \mathbf{d}) e^{\frac{1}{2}(z d^* - z^* d)}. \quad 81.$$

7.3. Kapit-Mueller model

In this section, we briefly describe the Kapit-Mueller (KM) model, which is a lattice model with an ideal band. We then illustrate how changing the orbital embedding can change the band from ideal to vortexable.

The KM model is a special type of Hofstadter model. Denoting the lattice vectors by $\mathbf{a}_{1,2}$, with unit cell area $|\mathbf{a}_1 \times \mathbf{a}_2| = 2\pi S$, each unit cell contains $\phi < 1$ flux. A general form of the Hofstadter Hamiltonian can be written as

$$H_{\text{Hof}} = \sum_{\mathbf{d} \in \Lambda} J(\mathbf{d}) t(\mathbf{d}), \quad 82.$$

where $\Lambda = \{m\mathbf{a}_1 + n\mathbf{a}_2\}$, $J(\mathbf{d})$ is a hopping term, and $t(\mathbf{d})$ is the magnetic translation operator. In the KM model, the hopping parameter exhibits Gaussian decay on the lattice, $J(\mathbf{d}) = \exp[-(1-\phi)\mathbf{d}^2 S]$. In this special case, the spectrum is non-negative with an exact flat band whose wavefunction is a LLL wavefunction sampled on lattice sites, i.e., $H_{\text{KM}}|\psi_{\mathbf{k}}\rangle = 0$, where the flat band wave function is given by

$$|\psi_{\mathbf{k}}\rangle = \sum_{\mathbf{r} \in \Lambda} \Phi_{\mathbf{k}}(\mathbf{r}) |\mathbf{r}\rangle, \quad 83.$$

where $\Phi_{\mathbf{k}}(\mathbf{r})$ is the LLL wavefunction and $|\mathbf{r}\rangle$ represents a localized orthonormal basis of states. As a consequence of its ideal band geometry, the KM model supports a Laughlin state of bosons at $\nu = 1/2$ as an exact ground state with on-site Hubbard repulsion (90).

We now demonstrate the importance of orbital embedding on the ideal band property of the KM model. For the KM model with flux $\phi = p/q < 1$, there are q orbitals in each

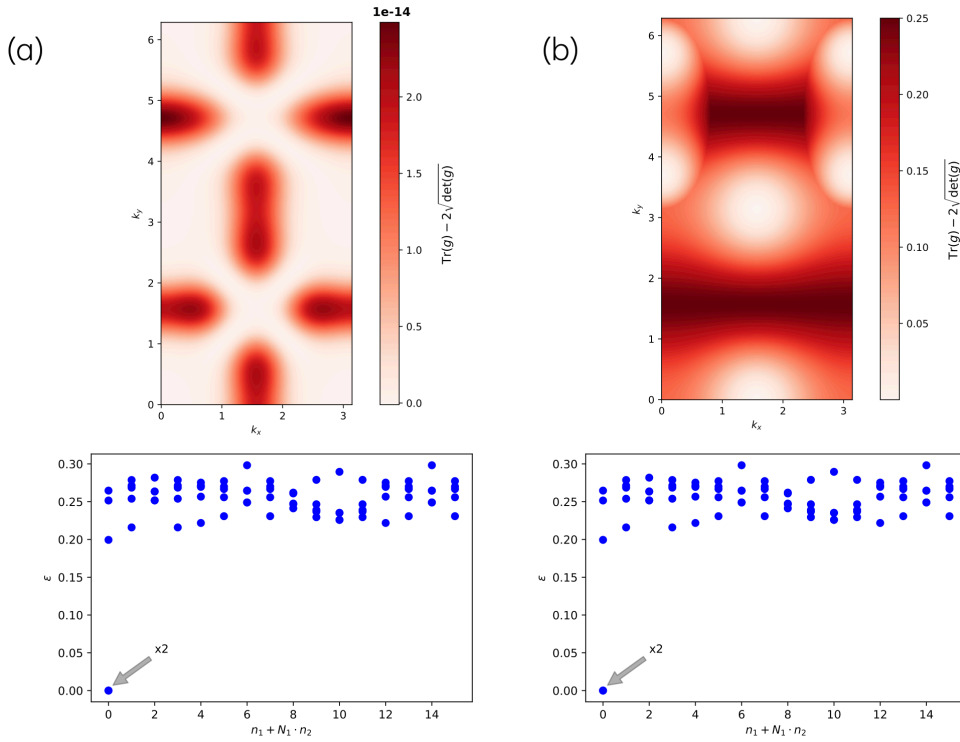


Figure 3

Deviation from the trace condition for the flat band in the KM model (top) and many-body spectrum with on-site Hubbard interaction (bottom) for the conventional orbital embedding (a) and an unconventional embedding (b). In the latter, the geometry is no longer ideal, but the many-body spectrum is unchanged.

magnetic unit cell. The standard description of the model equally spaces these orbitals within the unit cell. However, one can adjust their relative locations while keeping the magnetic unit cell unchanged, which amounts to tuning the orbital embedding. Tuning the embedding is also equivalent to adjusting the Fourier transform convention for different orbitals (31). As shown in Fig. 3, such a change ruins the ideal band property. However, since the Hubbard interaction is purely on-site, tuning the relative locations of the orbitals does not affect the many-body ground state – more concretely, the Laughlin state remains an exact zero-energy ground state after changing the embedding, despite violating the ideal band condition. The many-body spectrum is also shown in Fig. 3.

In fact, changing the embedding transforms the flat band of the Kapit-Mueller model from an ideal band to a vortexable but non-ideal band with a nontrivial vortex function $z(\mathbf{r})$. This underscores the point that the geometric properties of bands cannot alone predict the FCI ground state (101).